Advanced Functional Materials

ADVANCED FUNCTIONAL MATERIALS
www.afm-journal.de

RESEARCH ARTICLE

Synergistic Atomic-Vacancy Engineering in S-Scheme Heterojunction for Selective H_2O_2 Photosynthesis

Yamei Huang[1] | Jiayi Meng[1] | Yifan Liao[1] | Linlin Gao[1] | Yuchen Wei[1] | Quanmei Zhou[1] | Mohan Zhang[1] | Yuying Hu[1] | Baoning Zong[2] | Hexing Li[3] | Wei-Lin Dai[1]

[1]State Key Laboratory of Porous Materials for Separation and Conversion, Shanghai Key Laboratory of Molecular Catalysis and Innovative Materials, Department of Chemistry, Fudan University, Shanghai, P. R. China | [2]Research Institute of Petroleum Processing, Sinopec, Beijing, P. R. China | [3]Key Laboratory of Resource Chemistry of Ministry of Education, Shanghai Key Laboratory of Rare Earth Functional Materials, College of Chemistry and Materials Science, Shanghai Normal University, Shanghai, P. R. China

Correspondence: Baoning Zong (zongbn.ripp@sinopec.com) | Hexing Li (hexing-li@shnu.edu.cn) | Wei-Lin Dai (wldai@fudan.edu.cn)

Received: 29 January 2026 | **Revised:** 1 July 2026 | **Accepted:** 13 July 2026

Keywords: defect engineering | H_2O_2 production | interfacial charge dynamics | single-atom catalysis | S-scheme heterojunction

ABSTRACT

Solar-driven H_2O_2 production presents a sustainable alternative to the energy-intensive anthraquinone process, yet remains limited by inefficient charge transfer and poor selectivity. Herein, a synergistic strategy combining the atomic defect engineering and interfacial microenvironment modulation is established, which involves the in-situ mechanical growth of β-ketoenamine-linked covalent organic framework (TpBTD-COF) onto Zn single-atom-anchored sulfur-vacancy (S_v)-rich Sb_2S_3 nanorods (Zn-S_v/Sb_2S_3@TpBTD) to overcome the above limitations. The optimal Zn-S_v/Sb_2S_3@TpBTD-3 photocatalyst achieves a remarkable non-sacrificial H_2O_2 production rate of 2692 μmol g^{-1} h^{-1} with 90% selectivity in pure water, significantly outperforming most single-atom photocatalysts. Advanced characterizations and theoretical calculations indicate that the S_v-synergistic unsaturated Zn atomic sites as electron mediator under the internal electric field of S-scheme heterojunction optimizes the interfacial electron transfer and promotes O_2 adsorption, significantly improving activity and selectivity for H_2O_2 photosynthesis. This work offers an innovative perspective on the synergistic integration of defect engineering, single-atom catalysis, and heterojunction design for modulating the interfacial charge dynamics, enabling scalable solar-to-chemical energy conversion applications.

1 | Introduction

Hydrogen peroxide (H_2O_2) is a vital industrial chemical with diverse applications in chemical and medical industries [1, 2]. The conventional anthraquinone process currently dominates industrial H_2O_2 production but is plagued by intensive energy demands, hazardous emissions and safety risks [3–5]. Consequently, the mismatch between rising demand and unsustainable anthraquinone process has driven urgent efforts to exploit efficient alternatives for H_2O_2 production. Recent advances in solar-driven H_2O_2 production from naturally abundant H_2O and O_2 offer a promising route to achieve sustainable H_2O_2 production [6–10]. Nevertheless, the rational design of efficient photocatalysts featuring tailored active sites that simultaneously optimize charge dynamics and selectivity toward H_2O_2 production remains a critical challenge.

Single-atom catalysts (SACs) offer the potential for atomic-level tuning of oxygen reduction reaction (ORR) pathway via coordination and defect engineering [11–15]. Specifically, defect engineering modulates the local electronic structure to enhance O_2 activation, facilitate charge separation, and generate

low-coordination metal centers that stabilize O_2 adsorption and facilitate electron transfer [16, 17]. However, most studies overlook the critical role of semiconductor support in governing the electron structure of SACs during photocatalysis, leading to unsatisfactory H_2O_2 production activity in pure water and severely impeding the rational design of high-performance photocatalysts [18, 19]. To overcome these limitations, various strategies such as constructing heterojunctions and post-modifying structure have been employed to further improve the charge separation efficiency of SACs for boosting H_2O_2 photosynthesis [20]. Among potential semiconductor supports, antimony sulfide (Sb_2S_3) has attracted significant attention due to the suitable bandgap (~1.7 eV) and excellent optoelectronic properties, which makes it a promising platform for SACs [21–24]. The unique structure provides abundant anchoring sites that are crucial for stabilizing the single-atom metal centers and preventing their aggregation. The synergy between Sb_2S_3 and metal atomic sites may optimize interfacial electron transfer kinetics, thereby facilitating rapid charge separation and surface redox reactions. Unfortunately, few studies have explored the H_2O_2 photosynthesis of SACs-based Sb_2S_3, and the practical application is severely limited by severe charge carrier recombination, insufficient active sites and pronounced photocorrosion [25]. Constructing single-atom mediated heterojunctions utilizing Sb_2S_3 combined with ideal photocatalytic material such as COFs [26–28], may overcome aforementioned challenges, supporting optimized interfacial charge dynamics.

Herein, we propose an S-scheme heterojunction by in situ mechanical growth of β-ketoenamine-linked TpBTD-COF onto Zn single-atom-anchored S_v-rich Sb_2S_3 nanorods (Zn-S_v/Sb_2S_3@TpBTD) for efficient H_2O_2 photosynthesis. The optimal Zn-S_v/Sb_2S_3@TpBTD-3 exhibits a superior H_2O_2 production rate of 2692 μmol g^{-1} h^{-1} with 90% selectivity in pure water without any sacrificial agents, surpassing most of the previously reported SACs-based photocatalysts. Advanced characterizations combined with theoretical calculations reveal that the S_v-synergistic unsaturated Zn atomic sites as electron mediator under the internal electric field of S-scheme heterojunction optimizes the interfacial electron transfer and facilitate O_2 adsorption, significantly improving selectivity and efficiency for H_2O_2 photosynthesis. This work presents an innovative perspective on the synergistic integration of defect engineering, single-atom catalysis and heterojunction design, resolving charge dynamics and interfacial kinetics challenge.

2 | Results and Discussion

2.1 | Morphological and Structural Characterization

The Zn-S_v/Sb_2S_3@TpBTD heterostructure was synthesized through following fabrication steps (Figure 1a). First, Sb_2S_3 nanorods were synthesized by hydrothermal method and impregnated with zinc acetylacetonate, followed by calcination under N_2 to drive the anchoring of Zn single-atoms and S_v on the Sb_2S_3. Second, the TpBTD was in-situ grown on the Zn-S_v/Sb_2S_3 nanorods via mechanochemical synthesis to form the Zn-S_v/Sb_2S_3@TpBTD heterostructure. The composites with different proportions were obtained by adjusting the amount of Zn-S_v/Sb_2S_3 and denoted as Zn-S_v/Sb_2S_3@TpBTD-x (x = 1, 2, 3, 4, 5). Fourier transform infrared (FTIR) spectra provide clear evidence for the β-ketoenamine structure of TpBTD, with the characteristic stretching vibrations observed for C═O (1624 cm^{-1}) and C—N (1283 cm^{-1}) bonds, indicating the successful assembly of TpBTD (Figures S1 and S2) [29, 30]. The experimental x-ray diffraction (XRD) pattern of TpBTD matched well with the simulated pattern obtained using eclipsed ABC stacking model, indicating the TpBTD adopts a uniquely staggered ABC stacking mode (Figure S3) [31, 32]. Further XRD analysis reveals the identical diffraction patterns for Zn-S_v/Sb_2S_3 and pristine Sb_2S_3, demonstrating the absence of Zn aggregation. Raman spectra exhibit the asymmetric and symmetric stretching vibration at 276 and 301 cm^{-1} corresponding to the S—Sb bond, indicating that Zn single-atoms doping distorts the local S—Sb coordination environment that broadens the S—Sb Raman peak (Figure S4).

The morphology of as-prepared samples was confirmed by transmission electron microscopy (TEM) and scanning electron microscopy (SEM). The Sb_2S_3 exhibits uniform rod-like morphology, with the lattice spacing of 0.3 nm corresponding to the (211) facet (Figure 1b and Figure S5) [33]. Remarkably, the main lattice spacing of 0.8 nm corresponds to the (110) facet in Zn-S_v/Sb_2S_3, which has low-coordinated surface atoms and makes it easier to leave the lattice and form S_v (Figure 1c) [34, 35]. The absence of Zn particles/clusters in TEM image further supports the atomic dispersion of Zn in Zn-S_v/Sb_2S_3. Inductively coupled plasma mass spectrometry (ICP-MS) reveals that the content of Zn element in Zn-S_v/Sb_2S_3@TpBTD-3 catalyst is 0.71 wt.%. The Zn-S_v/Sb_2S_3@TpBTD-3 composite exhibits tight interface contact between Zn-S_v/Sb_2S_3 and TpBTD, confirming the formation of heterostructure (Figure 1d,e). Furthermore, Brunauer-Emmett-Teller (BET) tests indicate that the specific surface area of Zn-S_v/Sb_2S_3 is slightly higher than that of bulk Sb_2S_3, and Zn-S_v/Sb_2S_3@TpBTD-3 composite has further increased with the introduction of TpBTD, which provides abundant active sites and facilitates mass transfer (Figure S6). Aberration-corrected high-angle annular dark-field scanning transmission electron microscopy (AC-HAADF-STEM) was employed to confirm the atomic dispersion of Zn on Sb_2S_3 surface (Figure 1f,g). The marked spots in Sb_2S_3 lattice correspond to S_v, and the isolated low-contrast bright spots within well-ordered atomic lattice, corroborating the uniform distribution of Zn single-atoms (Figure 1h,i). Additionally, the electron paramagnetic resonance (EPR) spectroscopy indicates that Zn-S_v/Sb_2S_3 exhibits a distinct peak characteristic of S_v at g = 2.003 compared with Sb_2S_3, validating the successful introduction of S_v (Figure S7) [36]. Energy-dispersive x-ray spectroscopy (EDX) mapping reveals the uniform distribution of C, N, O, S, Sb, and Zn elements throughout the Zn-S_v/Sb_2S_3@TpBTD-3, confirming the uniform atomic dispersion of Zn (Figure 1j).

X-ray absorption near-edge spectroscopy (XANES) and extended x-ray absorption fine structure (EXAFS) spectra were conducted to investigate the atomic structure and coordination environment for Zn single-atoms in Zn-S_v/Sb_2S_3@TpBTD-3. The absorption edge position reveals that the valence state of Zn species is close to +2, consistent with the x-ray photoelectron spectroscopy (XPS) analysis (Figure 1k and Figure S8). EXAFS spectrum exhibits a prominent peak at 1.84 Å attributed to Zn—S bond, confirming

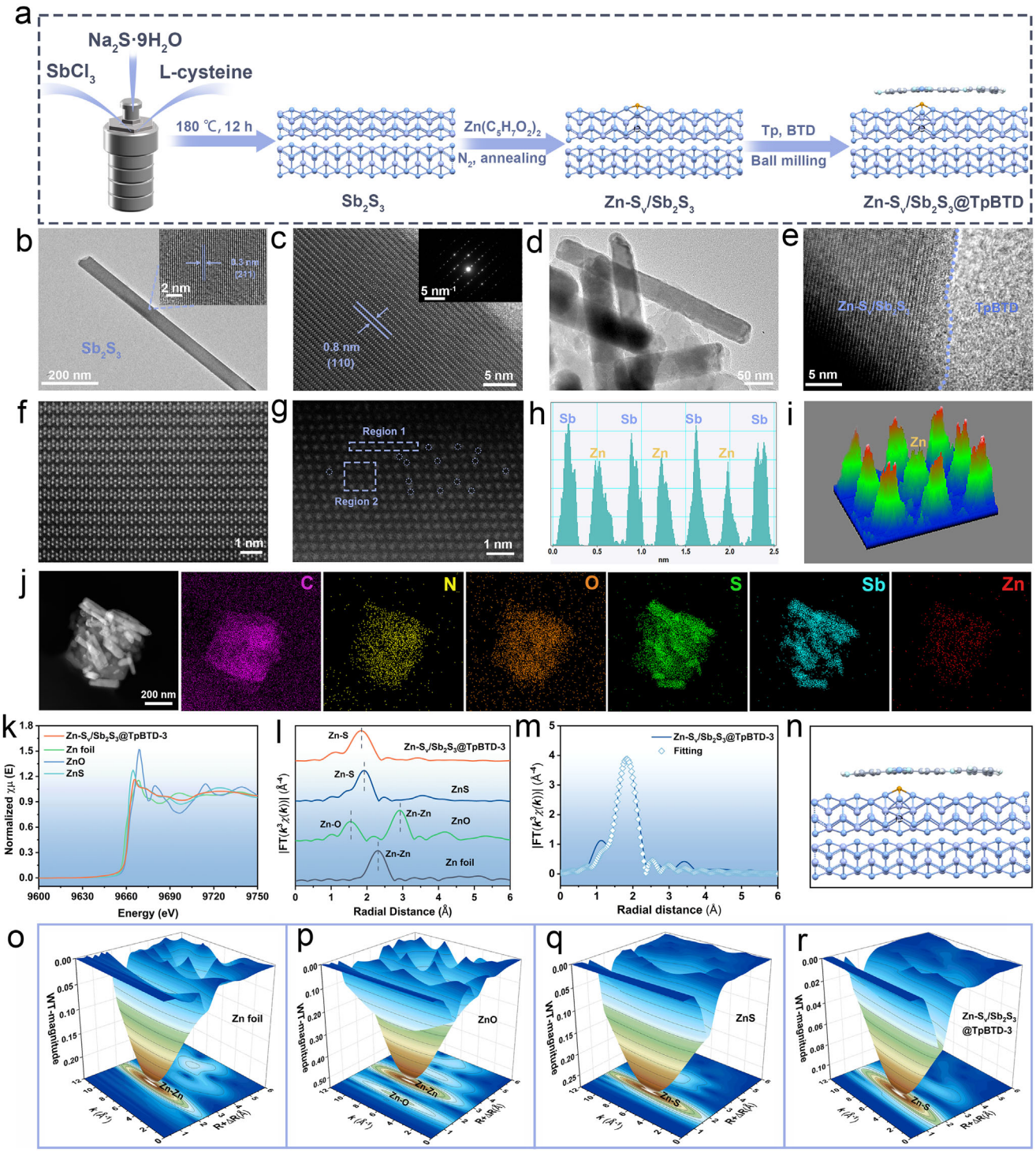

FIGURE 1 | (a) Schematic diagram of Zn-S_v/Sb_2S_3@TpBTD synthesis. TEM images of (b) Sb_2S_3, (c) Zn-S_v/Sb_2S_3, (d,e) Zn-S_v/Sb_2S_3@TpBTD-3. (f,g) AC-HAADF-STEM images of Zn-S_v/Sb_2S_3@TpBTD-3. (h) Linear atomic intensity profiles of region 1. (i) 3D atomic resolution map of region 2. (j) EDX mappings of Zn-S_v/Sb_2S_3@TpBTD-3. (k) XANES and (l) EXAFS spectra of Zn-S_v/Sb_2S_3@TpBTD-3 and reference. (m,n) EXAFS fitting curves and the possible structure of Zn-S_v/Sb_2S_3@TpBTD-3. (o–r) WT-EXAFS spectra of Zn-S_v/Sb_2S_3@TpBTD-3 and reference.

that the Zn species are stabilized by Zn—S coordination (Figure 1l) [37]. The comparison with Zn foil and ZnO references reveals the absence of Zn—Zn or Zn—O bond in Zn-S_v/Sb_2S_3@TpBTD-3, excluding the presence of Zn particles/clusters and confirming the atomic dispersion of Zn. EXAFS fitting further demonstrates the coordination numbers of Zn—S is approximate 3, implying an unsaturated coordination of Zn sites (Figure 1m,n). Wavelet transformed (WT) EXAFS spectra indicate that Zn-S_v/Sb_2S_3@TpBTD-3 exhibits a dominant peak at 5.94 $Å^{-1}$, corresponding to the Zn—S bond (Figure 1o–r). The signal of Zn-S_v/Sb_2S_3@TpBTD-3 displays an apparent deviation from that of ZnS, demonstrating an unsaturated coordination of Zn sites [38]. These results reveal

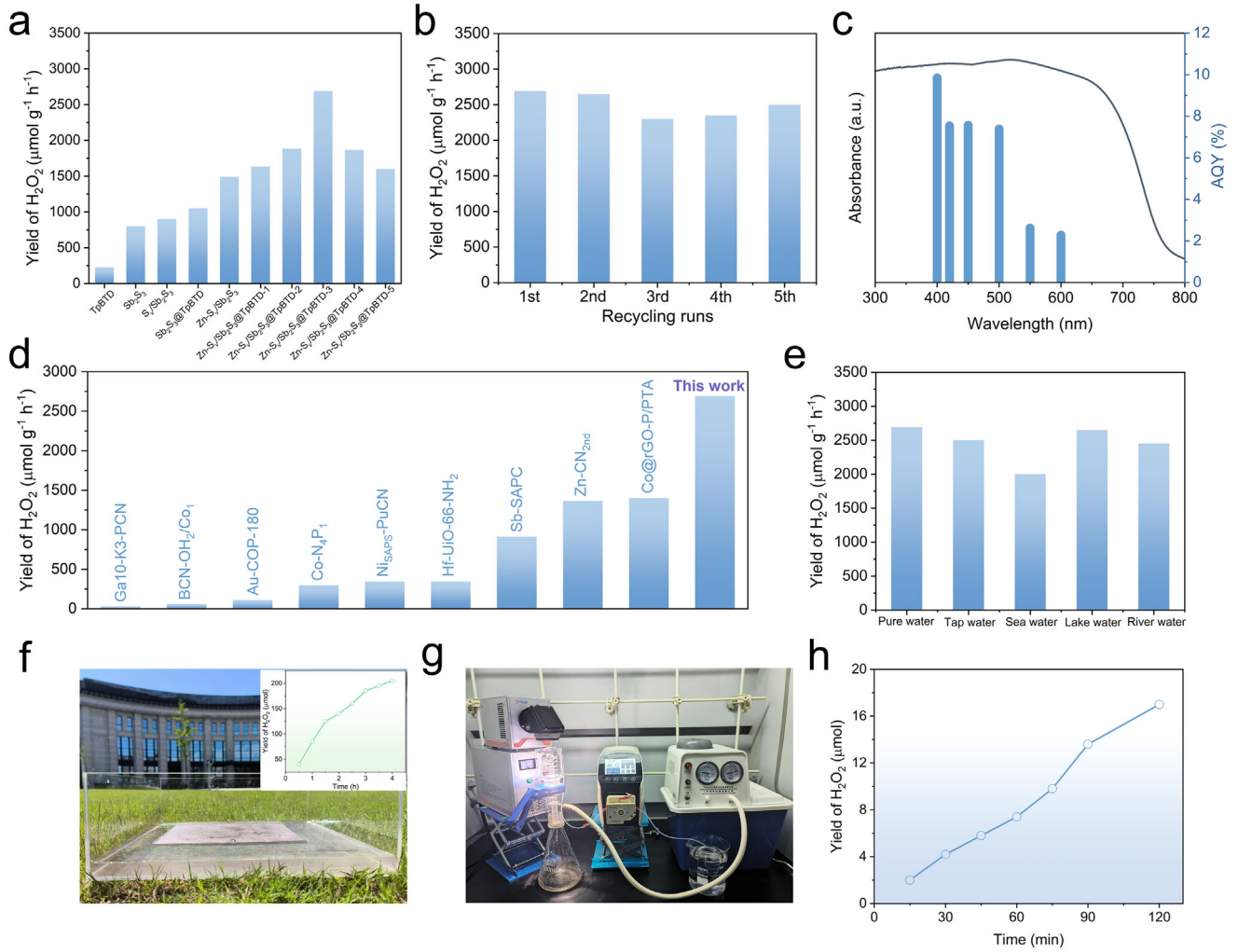

FIGURE 2 | (a) Photocatalytic performance of prepared catalysts. (b) Cyclic test of Zn-S_v/Sb_2S_3@TpBTD-3. (c) AQY of H_2O_2 photosynthesis over Zn-S_v/Sb_2S_3@TpBTD-3. (d) Comparison of previously reported single-atom photocatalysts. (e) H_2O_2 production in various types of real water sources. (f) H_2O_2 photoproduction under natural sunlight in Shanghai, Fudan University Jiangwan campus, July 1, 2025, sunny with abundant sunlight, temperature 37°C, using Zn-S_v/Sb_2S_3@TpBTD-3 loaded nonwoven fabric with 0.3 m^2, reactor containing 1 L pure water. (g,h) The continuous flow device and dynamic H_2O_2 production.

that S atoms within the Zn-S_v/Sb_2S_3@TpBTD-3 heterojunction serve as strong anchoring sites for Zn single-atoms, and the coordination structure of Zn is S_v-synergistic Zn-S_3 model.

2.2 | Performance of H_2O_2 Photosynthesis

H_2O_2 photosynthesis was conducted in O_2-saturated pure water without sacrificial agent under simulated sunlight, and quantified by iodometry (Figure S9). The photocatalytic activity of Sb_2S_3 with various Zn content indicates that Zn single-atoms play a positive role in H_2O_2 photosynthesis, which significantly enhances the production rate of H_2O_2 (Figure S10). The integration of Zn-S_v/Sb_2S_3 with TpBTD further promotes catalytic performance, with the optimized Zn-S_v/Sb_2S_3@TpBTD-3 photocatalyst achieving superior H_2O_2 production rate up to 2692 μmol g^{-1} h^{-1} (Figure 2a). Moreover, the H_2O_2 production rate of Zn-S_v/Sb_2S_3@TpBTD-3 remains nearly unchanged over 5 consecutive catalytic cycles, and the TEM, XRD, FTIR, and XPS patterns of the used catalyst remain almost unchanged, highlighting the exceptional operational and structural stability for Zn-S_v/Sb_2S_3@TpBTD-3 (Figure 2b and Figures S11–S14). The ICP analysis of the recovered catalyst reveals that the metal content remains nearly identical to that of the fresh sample, confirming the absence of significant metal leaching and the operational stability of Zn-S_v/Sb_2S_3@TpBTD-3 during the photocatalytic process (Table S1). In addition, the apparent quantum yield (AQY) and solar-to-chemical conversion (SCC) efficiency of Zn-S_v/Sb_2S_3@TpBTD-3 for photocatalytic H_2O_2 production illustrate that the AQY and SCC reached 9.85% at 400 nm and 0.26%, respectively (Figure 2c). The photocatalytic performance of Zn-S_v/Sb_2S_3@TpBTD-3 surpasses that of previously reported single-atom photocatalysts, further confirming the superiority (Figure 2d and Table S2). Meanwhile, the Zn-S_v/Sb_2S_3@TpBTD-3 maintains exceptional performance in various types of real water sources, suggesting the excellent potential for practical applications (Figure 2e). Benefiting from the high activity and flexibility, the Zn-S_v/Sb_2S_3@TpBTD-3 was engineered into membrane architecture for large-scale and continuous H_2O_2 production. The photocatalytic device was elaborately fabricated

by loading Zn-S_v/Sb_2S_3@TpBTD-3 catalyst onto polypropylene nonwoven fabric, confirming the feasibility of practical application potential. The Zn-S_v/Sb_2S_3@TpBTD-3 loaded nonwoven fabric photocatalyst effectively produces H_2O_2 up to 205 μmol in natural sunlight experiment, demonstrating the practical value for large-scale H_2O_2 photoproduction (Figure 2f). The continuous flow device also achieves excellent photocatalytic H_2O_2 production (Figure 2g,h).

2.3 | Charge Transfer and Separation Kinetics

To gain in-depth insight into the photocatalytic mechanism, the photogenerated carrier separation and transfer dynamics of catalysts was investigated by steady-state photoluminescence (PL) spectroscopy and time-resolved photoluminescence (TRPL) spectroscopy. The Zn-S_v/Sb_2S_3 exhibits the lowest PL emission intensity, and further assembly with TpBTD obtained Zn-S_v/Sb_2S_3@TpBTD-3 composite with lower PL emission intensity, indicating the enhanced charge separation (Figure 3a) [39, 40]. The average fluorescence lifetimes of TpBTD, Sb_2S_3, Zn-S_v/Sb_2S_3 and Zn-S_v/Sb_2S_3@TpBTD-3 were determined by TRPL spectroscopy to be 1.13, 1.91, 2.05, and 2.18 ns, respectively, indicating the efficient separation of photogenerated carriers in Zn-S_v/Sb_2S_3@TpBTD-3 heterostructure (Figure 3b) [41]. The above results confirm that the incorporation of S_v-synergistic unsaturated Zn single-atoms, combined with heterojunction engineering can effectively optimize the electronic structure and significantly improve the separation and transfer efficiency of photogenerated carriers. The improved carrier dynamics was further investigated through photoelectrochemical measurements. Electrochemical impedance spectroscopy (EIS) and transient photocurrent response indicate that the Zn-S_v/Sb_2S_3@TpBTD-3 exhibits the lowest impedance and highest transient photocurrent density, implying the incorporation of S_v-synergistic unsaturated Zn single-atoms, combined with heterojunction engineering can effectively facilitate intrinsic electron transfer (Figure 3c,d) [42]. The direction of electron transfer in Zn-S_v/Sb_2S_3@TpBTD-3 heterojunction was further investigated using in situ irradiated XPS (ISI-XPS). The peak of N 1s shift by 0.1 eV toward lower binding energy when the Zn-S_v/Sb_2S_3 and TpBTD is contacted, indicating a significant increase in electron density within the TpBTD. The S 2p, Sb 3d, and Zn 2p peaks of Zn-S_v/Sb_2S_3@TpBTD-3 exhibit a positive shift of 0.1 eV compared to those of Zn-S_v/Sb_2S_3, attributed to the strong interfacial interaction between Zn-S_v/Sb_2S_3 and TpBTD (Figure S15). The observed positive shift in the N 1s binding energy under illumination reflects electron depletion in TpBTD, while the contrastive negative shift in the S 2p and Sb 3d peaks of Zn-S_v/Sb_2S_3 suggests electron accumulation, providing the photoinduced interfacial charge transfer from TpBTD to Zn-S_v/Sb_2S_3. The negative shift in Zn 2p binding energy indicates enhanced electron density, establishing the role of Zn single-atom sites as the final electron acceptor and further modulating interfacial electron dynamics (Figure 3e–h) [43]. The charge transfer mechanism within Zn-S_v/Sb_2S_3@TpBTD-3 heterojunction was further investigated by ISI-XPS with tunable single-wavelength illumination (375, 405, 450, 520, and 589 nm) (Figure 3i). The analysis reveals that the binding energy of Zn 2p under 375 nm illumination exhibits a negative shift of 0.34 eV compared with dark condition, as illumination shifted from low-energy (589 nm) to high-energy (375 nm) radiation with charge compensation [44]. The wavelength-dependent shift indicates that photon energy directly influences photoexcited electron migration, modulating the local electron density of Zn single-atom sites and enhancing the redox capability of Zn-S_v/Sb_2S_3@TpBTD-3 heterostructure. The photoreduction deposition of Au nanoparticles was further performed using $HAuCl_4$ as the precursor. TEM images reveal that the Au nanoparticles are selectively deposited on the Zn-S_v/Sb_2S_3 component, indicating that it serves as the primary reduction site, and supports the S-scheme mechanism (Figure S16). The above analyses clearly demonstrate the electron transfer from Zn-S_v/Sb_2S_3 to TpBTD within Zn-S_v/Sb_2S_3@TpBTD-3 heterojunction, and photogenerated electron flow in the opposite direction under illumination, consistent well with the S-scheme mechanism.

To explore the mechanism underlying superior photocatalytic performance, ultraviolet photoelectron spectroscopy (UPS) was performed using He I as the excitation source. As depicted in Figure 3j–l, the work function of Zn-S_v/Sb_2S_3 (3.76 eV) is lower than that of TpBTD (4.05 eV), while Zn-S_v/Sb_2S_3@TpBTD-3 (3.89 eV) intermediates between the two components, indicating the interfacial band bending within heterojunction. The band structure diagram is obtained by optical bandgap and Mott–Schottky diagram, further demonstrating that the TpBTD and Zn-S_v/Sb_2S_3 satisfy thermodynamics potential for $2e^-$ ORR (Figure 3m and Figures S17–S22) [45–49]. The charge transfer mechanism of Zn-S_v/Sb_2S_3@TpBTD-3 S-scheme heterojunction indicates that the electrons tend to transfer from Zn-S_v/Sb_2S_3 to TpBTD upon contact, until the Fermi levels reach equilibrium (Figure 3n). Due to the electron depletion and accumulation on Zn-S_v/Sb_2S_3 and TpBTD surface, respectively, an internal electric field (IEF) is formed that causes the band edge of Zn-S_v/Sb_2S_3 and TpBTD to bend upward and downward, respectively. Under simulated sunlight irradiation, the IEF and band edge bending drive the recombination of photogenerated electrons in the conduction band (CB) of TpBTD with holes in the valence band (VB) of Zn-S_v/Sb_2S_3, and through S_v-synergistic unsaturated Zn single-atoms as electron mediator under the IEF, optimizing interfacial electron transfer. The S-scheme charge transfer pathway in Zn-S_v/Sb_2S_3@TpBTD-3 heterojunction simultaneously enhances the charge separation efficiency and redox capacity.

The charge transfer dynamics was further elucidated by femtosecond transient absorption spectroscopy (fs-TAS). The TpBTD exhibits a pronounced negative signal, which is characteristic of ground-state bleaching (GSB), attributing to the generation and subsequent quenching of photogenerated electrons. Notably, the Zn-S_v/Sb_2S_3@TpBTD-3 heterojunction exhibits an excited-state absorption (ESA), attributed to the excited-state arising from the strong electronic interaction at interface, and offers direct spectral evidence for interfacial charge transfer (Figure 4a–d) [50]. Based on the decay kinetics and fitted average lifetimes, the Zn-S_v/Sb_2S_3@TpBTD-3 possesses a longer average carrier lifetime (τ_{avg}) compared to that of pristine TpBTD (Figure 4e,f). The decay curve of the original TpBTD is fitted using double-exponential model, including a fast lifetime (τ_1 = 0.50 ps) for the electron transfer process from the CB to trapping state (TS) and a slow lifetime (τ_2 = 141 ps) for radiative recombination process [51]. For Zn-S_v/Sb_2S_3@TpBTD-3, the decay curves can be fitted by three-exponential model that the shortest lifetime (τ_1 = 0.16 ps) assigned to electron transfer from the TpBTD to Zn-S_v/Sb_2S_3,

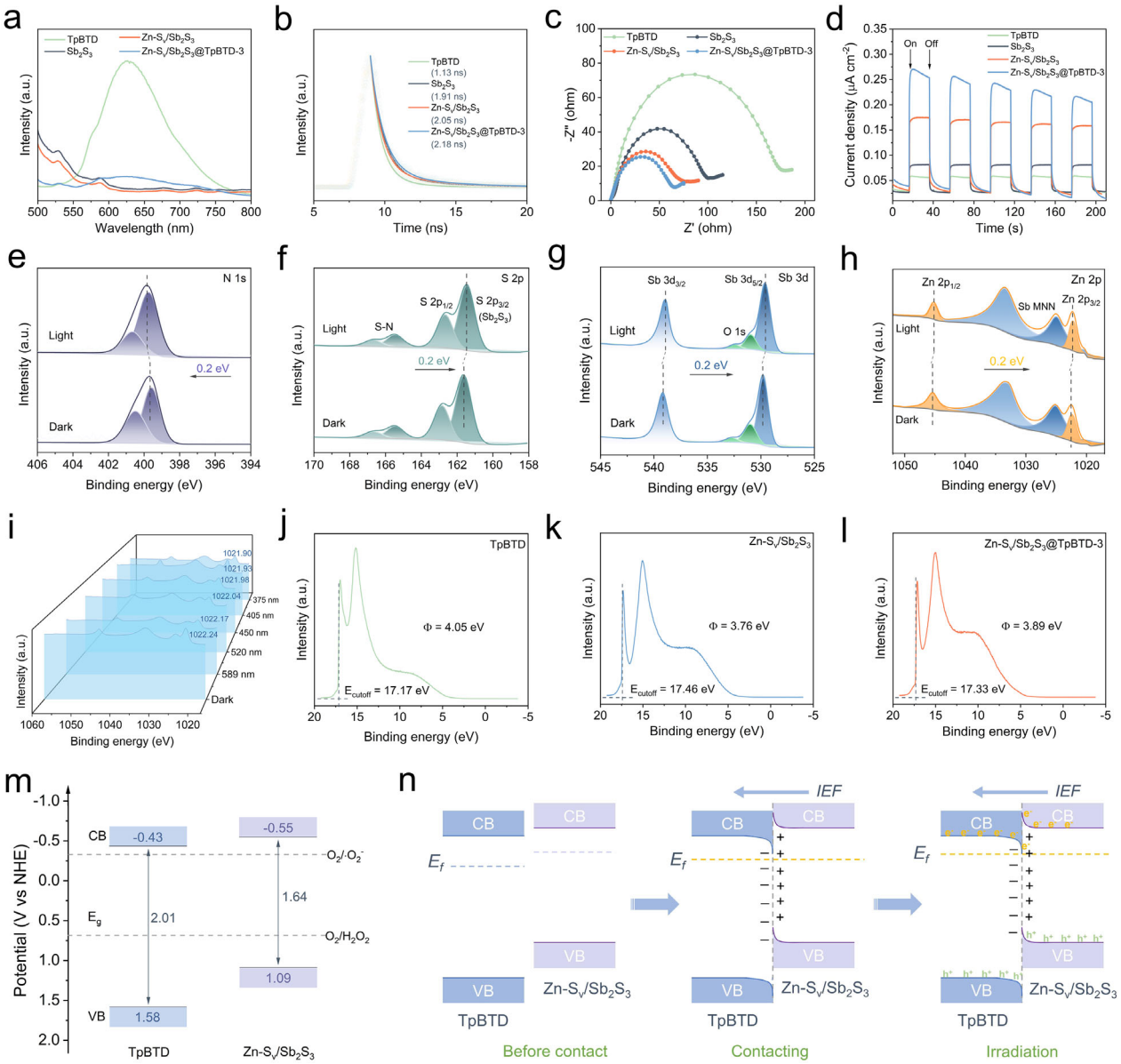

FIGURE 3 | (a,b) PL and TRPL spectra, (c,d) EIS Nyquist plots and transient photocurrent response curves of TpBTD, Sb_2S_3, Zn-S_v/Sb_2S_3, Zn-S_v/Sb_2S_3@TpBTD-3. (e–h) ISI-XPS spectra of Zn-S_v/Sb_2S_3@TpBTD-3. (i) ISI-XPS spectra of Zn 2p under different wavelength light irradiation. (j–l) UPS spectra of TpBTD, Zn-S_v/Sb_2S_3 and Zn-S_v/Sb_2S_3@TpBTD-3. (m) The diagram of the band structure. (n) Schematic illustration of IEF formation.

owing to the presence of strong IEF in the heterojunction. As compared with TpBTD, the Zn-S_v/Sb_2S_3@TpBTD-3 possesses much faster electron transfer (τ_2 = 4.58 ps) from CB to TS, which is ascribed to the presence of abundant S_v-synergistic unsaturated Zn single-atoms, providing a stronger driving force to accelerate charge migration [52, 53]. In addition, the Zn-S_v/Sb_2S_3@TpBTD-3 possesses much longer lifetime (τ_3 = 856 ps) for direct charge recombination than TpBTD, confirming the prolonged lifetime and inhibited recombination of the photogenerated charge carriers, which will facilitate optimized charge transfer within the S-scheme heterojunction through precisely engineered interface.

To further investigate the reaction pathway over Zn-S_v/Sb_2S_3@TpBTD-3 heterostructure, H_2O_2 production was evaluated under different atmospheric conditions and scavengers (Figure 4g). The H_2O_2 evolution rate is significantly inhibited under Ar atmosphere, confirming that H_2O_2 is generated exclusively through the ORR process. Moreover, H_2O_2 production rate decreases after the addition of benzoquinone (BQ) for superoxide radical ($\bullet O_2^-$) scavenger, indicating that the 2e$^-$ ORR is predominant pathway with $\bullet O_2^-$ serving as key intermediate [54–56]. The EPR measurement was conducted to probe reactive intermediates, revealing the existence of DMPO-$\bullet O_2^-$ signals under light irradiation (Figure 4h). To further illustrate the reaction process accurately, in-situ diffuse reflectance infrared Fourier transform spectroscopy (DRIFTS) was applied to identify the real-time intermediates during H_2O_2 photoproduction (Figure 4i). The signals of $*O_2^-$ (1184 cm^{-1}) and *OOH (1278 cm^{-1}) gradually intensified with extended light exposure, accompanied by the emergence of characteristic peak for adsorbed H_2O_2 (1373 cm^{-1}), confirming that O_2 is reduced via 2e$^-$ ORR pathway

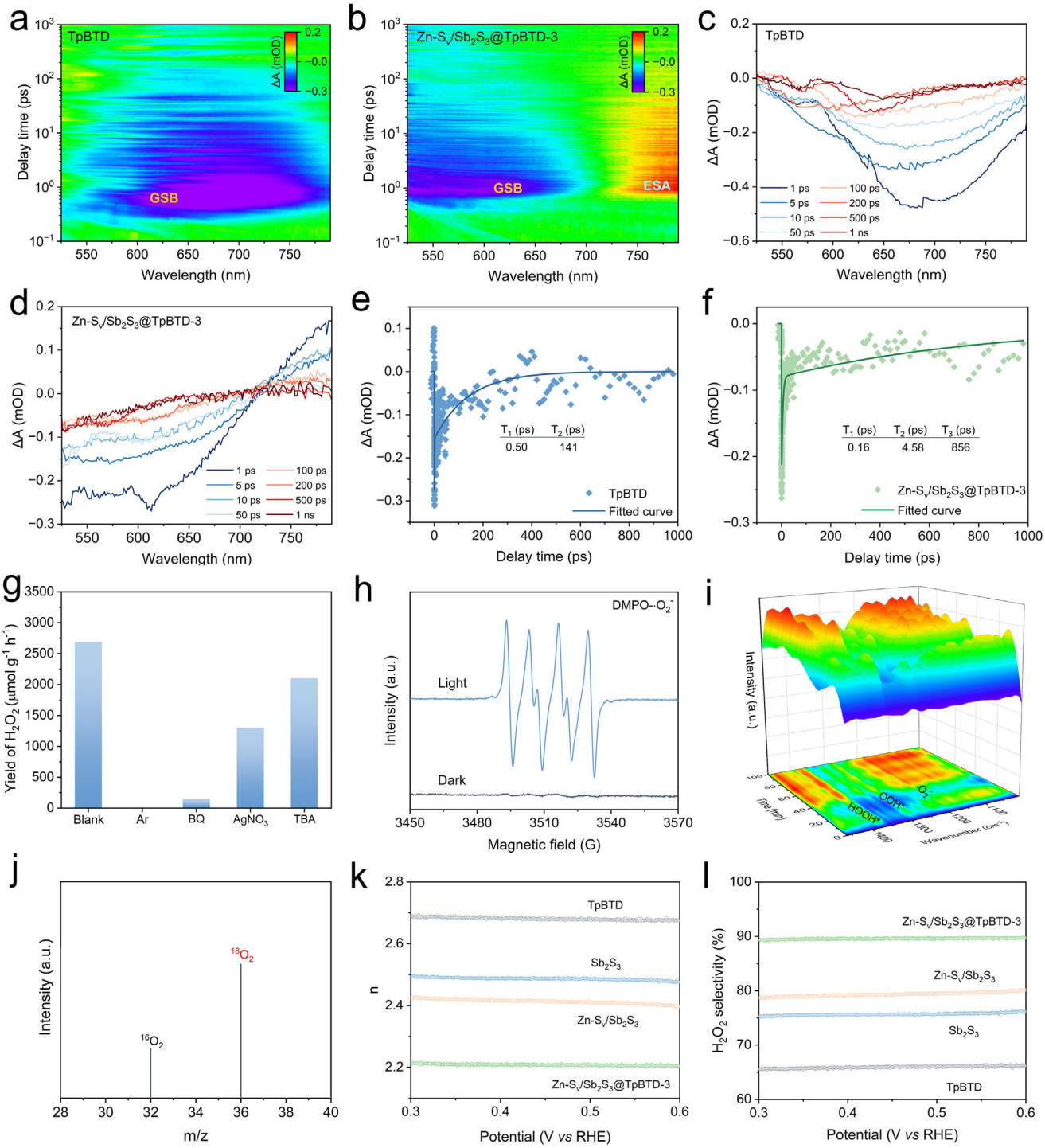

FIGURE 4 | (a,b) Contour maps of fs-TAS spectra for TpBTD and Zn-S_v/Sb_2S_3@TpBTD-3. (c,d) Transient absorption spectra recorded at indicated delay time. (e,f) Normalized decay kinetic curves. (g) H_2O_2 production over Zn-S_v/Sb_2S_3@TpBTD-3 with various scavengers. (h) The EPR spectra of Zn-S_v/Sb_2S_3@TpBTD-3. (i) In situ DRIFTS spectra of Zn-S_v/Sb_2S_3@TpBTD-3 under light irradiation. (j) Mass spectrometry of reaction products using isotope-labeled $^{18}O_2$. (k) The electron transfer number and selectivity of H_2O_2 production.

and form $*O_2^-$ and *OOH, which is further converted to H_2O_2 [57–59]. The reaction pathway is further investigated by isotope-labeling experiment, in which the detection of $^{18}O_2$ (a small amount of $^{16}O_2$ originates from air) demonstrates that H_2O_2 is produced via the ORR pathway (Figure 4j). The $2e^-$ ORR process is confirmed by the rotating ring-disk electrode (RRDE) measurements, which suggests the electron transfer number of Zn-S_v/Sb_2S_3@TpBTD-3 is closer to 2, indicating the superiority in H_2O_2 photosynthesis (Figure 4k). Additionally, the Zn-S_v/Sb_2S_3@TpBTD-3 exhibits a remarkable H_2O_2 selectivity up to 90%, further confirming the domination of $2e^-$ ORR pathway (Figure 4l).

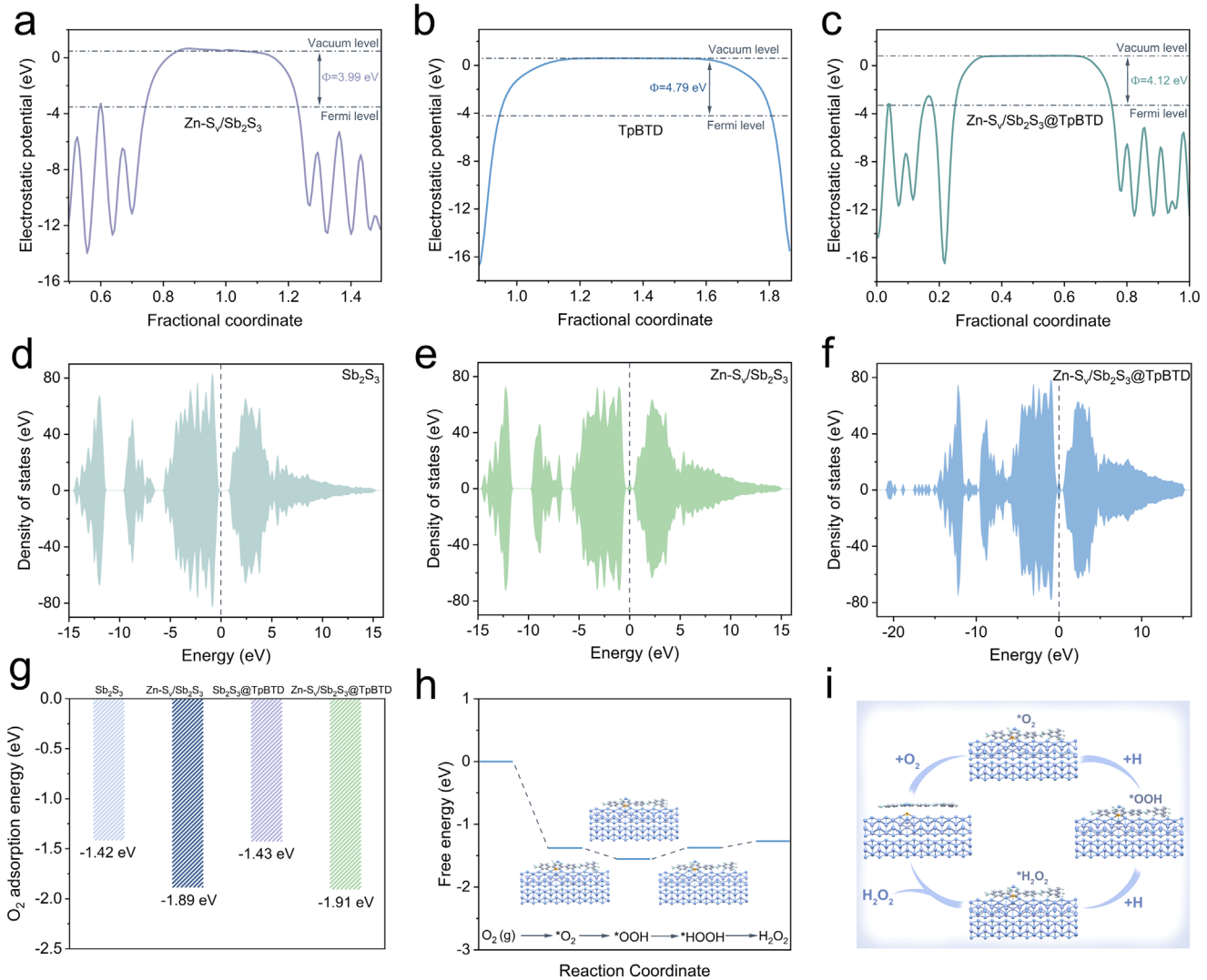

FIGURE 5 | Theoretical work function of (a) Zn-S_v/Sb_2S_3, (b) TpBTD, (c) Zn-S_v/Sb_2S_3@TpBTD. The DOS of (d) Sb_2S_3, (e) Zn-S_v/Sb_2S_3, (f) Zn-S_v/Sb_2S_3@TpBTD. (g) Optimum O_2 adsorption energy of Sb_2S_3, Zn-S_v/Sb_2S_3, Sb_2S_3@TpBTD and Zn-S_v/Sb_2S_3@TpBTD. (h) The free energy diagram, (i) Schematic illustration for H_2O_2 photosynthesis on Zn-S_v/Sb_2S_3@TpBTD.

2.4 | Mechanism Analysis

Density functional theory (DFT) calculations were performed to elucidate the mechanism by which Zn-S_v/Sb_2S_3@TpBTD heterojunction promoted H_2O_2 photoproduction. The work function for Zn-S_v/Sb_2S_3, TpBTD and Zn-S_v/Sb_2S_3@TpBTD are determined to be 3.99, 4.79, and 4.12 eV, respectively (Figure 5a–c). The higher work function of TpBTD indicates that the electrons will transfer from Zn-S_v/Sb_2S_3 to TpBTD when in close contact with each other, consistent with the XPS and UPS results [60, 61]. The differential charge density distribution of Zn-S_v/Sb_2S_3@TpBTD heterostructure indicates that the planar-averaged charge density difference along with Z direction exhibits the change of charge density, revealing the electrons mainly transfer from Zn-S_v/Sb_2S_3 to TpBTD (Figure S23) [62]. Under illumination, the photogenerated electrons on the CB of TpBTD are driven to combine with the holes on the VB of Zn-S_v/Sb_2S_3 through S_v-synergistic unsaturated Zn single-atoms as electron mediator under the internal electric field. Furthermore, the comparison for density of states (DOS) of Sb_2S_3 and the incorporation of S_v-synergistic unsaturated Zn single-atoms reveals that a significant increase in electron density near the Fermi level in Zn-S_v/Sb_2S_3. The electron density is further increased upon formation of Zn-S_v/Sb_2S_3@TpBTD composite, which promotes charge transfer kinetics, resulting in superior catalytic activity for H_2O_2 production (Figure 5d–f and Figure S24).

DFT calculations were further conducted to achieve a more comprehensive understanding for the fundamental processes of H_2O_2 photoproduction at the atomic scale. The adsorption energy of O_2 on Zn-S_v/Sb_2S_3@TpBTD (−1.91 eV) is more negative compared to that of Sb_2S_3 (−1.42 eV), Zn-S_v/Sb_2S_3 (−1.89 eV) and Sb_2S_3@TpBTD (−1.43 eV), confirming the higher stability of O_2 molecules adsorbed on the Zn-S_v/Sb_2S_3@TpBTD heterostructure (Figure 5g) [63, 64]. The temperature-programmed desorption of O_2 (O_2-TPD) similarly demonstrates the enhanced O_2 chemisorption ability for Zn-S_v/Sb_2S_3@TpBTD composite (Figures S25 and S26). The analysis indicates that the introduction of S_v-synergistic unsaturated Zn single-atoms significantly enhances the adsorption capacity for O_2 molecules and serves as the active site driving

the subsequent ORR process (Figure S27). Therefore, the Zn-S_v/Sb_2S_3@TpBTD exhibits prominent advantage for the first step (O_2 adsorption) of 2e$^-$ ORR process. The free energy changes for photocatalytic 2e$^-$ ORR on Zn-S_v/Sb_2S_3@TpBTD heterostructure are further calculated, and the optimized surface intermediates together with the corresponding free energy changes for each step of H_2O_2 production is shown in Figure 5h. The reaction process includes the following steps: 1) adsorption of O_2 molecules on the active sites to form adsorbed *O_2; 2) transfer of electrons to the adsorbed *O_2 and reduce to *OOH; 3) combination of H^+ with *OOH to form *HOOH; and 4) hydrogenation of *HOOH to form H_2O_2 (Figure 5i) [65, 66]. The theoretical results are consistent with experimental observations, indicating the outstanding intrinsic activity of Zn-S_v/Sb_2S_3@TpBTD S-scheme heterojunction for selective H_2O_2 production.

3 | Conclusion

In summary, an S-scheme heterojunction photocatalyst constructed by in-situ mechanical growth of TpBTD onto Zn single-atom-anchored S_v-rich Sb_2S_3 nanorods (Zn-S_v/Sb_2S_3@TpBTD), enables highly selective H_2O_2 photoproduction. The optimal Zn-S_v/Sb_2S_3@TpBTD-3 photocatalyst achieves a remarkable H_2O_2 production rate of 2692 μmol g^{-1} h^{-1} with 90% selectivity in pure water without sacrificial agent, which significantly outperforming most reported single-atom photocatalytic systems. Comprehensive analyses including AC-HAADF-STEM, EXAFS, fs-TAS and DFT calculations, provide in-depth insights into mechanism that the S_v-synergistic unsaturated Zn atomic sites as electron mediator under the internal electric field of S-scheme heterojunction optimize the interfacial electron transfer and promote O_2 adsorption, significantly improving selectivity and efficiency for H_2O_2 photosynthesis. This work presents an innovative perspective on constructing defect engineering and single-atoms mediated heterojunctions, enabling efficient and scalable photocatalytic H_2O_2 production.

Acknowledgements

This work was supported by the National Key Research and Development Program of China (2021YFA1501404), and the Science and Technology Commission of Shanghai Municipality (2024ZDSYS02).

Conflicts of Interest

The authors declare no conflicts of interest.

Data Availability Statement

The data that support the findings of this study are available from the corresponding author upon reasonable request.

References

1. F. Yang, C. Feng, S. Zuo, et al., "Photocatalytic H_2O_2 Production with >30% Quantum Efficiency via Monovalent Copper Dynamics," *Journal of the American Chemical Society* 147 (2025): 17112–17120.

2. Y. Zhang, C. Pan, G. Bian, et al., "H_2O_2 Generation from O_2 and H_2O on a Near-Infrared Absorbing Porphyrin Supramolecular Photocatalyst," *Nature Energy* 8 (2023): 361–371.

3. C. Feng, J. Alharbi, M. Hu, et al., "Ultrafast Charge Transfer on Ru-Cu Atomic Units for Enhanced Photocatalytic H_2O_2 Production," *Advanced Materials* 37 (2025): 2406748.

4. Z. Zhang, Y. Hou, S. Zhu, et al., "Benzotrifuran-Based Covalent Organic Frameworks for Artificial Photosynthesis of H_2O_2 from H_2O, O_2, and Sunlight," *Angewandte Chemie International Edition* 64 (2025): 202505286.

5. M. Liu, Y. Xu, Y. Liu, et al., "Constructing Large-Area Oriented Covalent Organic Framework Based PN Heterostructure Films to Enhance Artificial Photosynthesis of H_2O_2," *Angewandte Chemie International Edition* 64 (2025): 202505491.

6. C. Shi, R. Pan, J. Yuan, and C. Liu, "Elucidating Unique Synergic Enhancement Effect for H_2O_2 Production in Crystalline Carbon Nitride with Cyanamide-Defect and Heptazine-Triazine Junction," *Advanced Functional Materials* 35 (2025): 2500342.

7. Y. Hou, F. Liu, J. Liang, Z. Li, P. Zhou, and M. Tong, "Building a Confluence Charge Transfer Pathway in COFs for Highly Efficient Photosynthesis of Hydrogen Peroxide from Water and Air," *Angewandte Chemie International Edition* 64 (2025): 202505621.

8. X. Ruan, C. Ding, J. Leng, et al., "Decoupling of Carrier Pathways in Au/Cu-$Zn_3In_2S_6$ Through Bulk Hole Trapping and Surface Hot Electron Accumulation Enhances Photocatalytic Hydrogen Peroxide Production," *Advanced Materials* 37 (2025): 11422.

9. B. Yu, S. Liu, X. Lin, et al., "Breathing Air into Water: Dual-Pathway H_2O_2 Synthesis Via Aerating Amphiphilic Supramolecular Films," *Energy & Environmental Science* 18 (2025): 8382–8390.

10. J. R. Huang, H. Y. Chen, H. L. Zhu, P. Q. Liao, and X. M. Chen, "Ni-Zn Dual-Atom Sites Enable Synergistic Parallel Pathways for Efficient Photosynthesis of H_2O_2 with Long-Term Stability," *Journal of the American Chemical Society* 147 (2025): 37167–37175.

11. Y. Li, D. Luan, and X. W. Lou, "Engineering of Single-Atomic Sites for Electro- and Photo-Catalytic H_2O_2 Production," *Advanced Materials* 36 (2024): 2412386.

12. Z. Teng, Q. Zhang, H. Yang, et al., "Atomically Dispersed Antimony on Carbon Nitride for the Artificial Photosynthesis of Hydrogen Peroxide," *Nature Catalysis* 4 (2021): 374–384.

13. X. Zhang, H. Su, P. Cui, et al., "Developing Ni Single-Atom Sites in Carbon Nitride for Efficient Photocatalytic H_2O_2 Production," *Nature Communications* 14 (2023): 7115.

14. Y. Kondo, K. Honda, Y. Kuwahara, K. Mori, H. Kobayashi, and H. Yamashita, "Boosting Photocatalytic Hydrogen Peroxide Production from Oxygen and Water Using a Hafnium-Based Metal-Organic Framework with Missing-Linker Defects and Nickel Single Atoms," *ACS Catalysis* 12 (2022): 14825–14835.

15. H. Ou, Y. Jin, B. Chong, et al., "Hydroxyl-Bonded Co Single Atom Site on Boroncarbonitride Surface Realizes Nonsacrificial H_2O_2 Synthesis in the Near-Infrared Region," *Advanced Materials* 36 (2024): 2404851.

16. W. Xie, J. Liu, and X. H. Liu, "N Vacancies Modulated Zn Single Atoms for Efficient H_2O_2 Photosynthesis," *Journal of Materials Chemistry A* 12 (2024): 19497–19503.

17. Z. Gao, F. Liu, Z. Chen, et al., "Defect-Modulated Oxygen Adsorption and Z-Scheme Charge Transfer for Highly Selective H_2O_2 Photosynthesis in Pure Water," *Nature Communications* 16 (2025): 8889.

18. C. Fu, Y. Wang, L. Xu, et al., "Axial Ligand Engineering of Silver Single-Atom Catalysts with NHeterocyclic Carbenes Unlocks Efficient Photocatalytic H_2O_2 Production," *Journal of the American Chemical Society* 148 (2026): 280–291.

19. X. Ruan, M. Xu, C. Ding, et al., "Cd Single Atom as an Electron Mediator in an S-Scheme Heterojunction for Artificial Photosynthesis of H_2O_2," *Advanced Energy Materials* 15 (2025): 2405478.

20. C. Ding, S. Zhao, X. Ruan, et al., "Reverse Charge Transfer Drives d-p Orbital Hybridization in Ruthenium-Oxygen Modified $Zn_3In_2S_6$ for Hydrogen Peroxide Photosynthesis," *Advanced Materials* 37 (2025): 09867.

21. S. Chamola, R. Zhou, O. M. Bakr, and S. Ahmad, "Sb_2S_3 Nanorods for Photoenhanced Li-Ion Batteries: A Synergetic Balance Between Energy Harvesting and Storage," *Advanced Functional Materials* 35 (2024): 2414913.

22. Y. Wang, M. Jin, Z. Wan, et al., "PbSe-Induced Sb_2S_3 Crystallization and Interface Band Optimization for High-Efficiency Bulk Heterojunction Sb_2S_3 Solar Cells," *Advanced Functional Materials* 35 (2025): 2420361.

23. J. Chen, G. Li, Z. Xu, et al., "Recent Advances and Prospects of Solution-Processed Efficient Sb_2S_3 Solar Cells," *Advanced Functional Materials* 34 (2024): 2313676.

24. Y. Wang, D. Yang, M. Jin, et al., "Full-Dimensional Penetration Strategy with Degradable PEAI Enables 8.21% Efficiency in Bulk Heterojunction Sb_2S_3 Solar Cells," *Advanced Energy Materials* 15 (2025): 2502805.

25. L. Wang, F. Guo, S. Ren, R. T. Gao, and L. Wu, "Unbiased Photoelectrochemical H_2O_2 Coupled to H_2 Production via Dual Sb_2S_3-Based Photoelectrodes with Ultralow Onset Potential," *Angewandte Chemie International Edition* 63 (2024): 202411305.

26. K. H. Xie, G. B. Wang, F. Huang, et al., "Multicomponent One-Pot Construction of Benzo[f]Quinoline-Linked Covalent Organic Frameworks for H_2O_2 Photosynthesis," *Nature Communications* 16 (2025): 3493.

27. S. Yang, D. Si, L. Zou, M. Shi, Y. Huang, and R. Cao, "Engineering Imine Carbon Catalytic Sites in Covalent Organic Frameworks for Enhanced Overall H_2O_2 Photosynthesis," *Journal of the American Chemical Society* 147 (2025): 30287–30295.

28. Z. Chen, H. Weng, C. Chu, et al., "Nitrogen Heterocyclic Covalent Organic Frameworks for Efficient H_2O_2 Photosynthesis and in Situ Water Treatment," *Nature Communications* 16 (2025): 6943.

29. X. Li, S. Yang, F. Zhang, L. Zheng, and X. Lang, "Facile Synthesis of 2D Covalent Organic Frameworks for Cooperative Photocatalysis with TEMPO: The Selective Aerobic Oxidation of Benzyl Amines," *Applied Catalysis B: Environmental* 303 (2022): 120846.

30. H. Zhao, Y. Wang, F. Zhang, X. Dong, and X. Lang, "Oxygen-Atom Substitution in a β-Ketoenamine-Linked Covalent Organic Framework for Boosting Photocatalytic Oxygenation of Sulfides," *Applied Catalysis B: Environment and Energy* 350 (2024): 123899.

31. S. Yang, T. Li, Y. Cheng, et al., "Covalent Organic Framework Isomers for Photoenhanced Gold Recovery from EWaste with High Efficiency and Selectivity," *ACS Sustainable Chemistry & Engineering* 10 (2022): 9719–9731.

32. S. Yang, X. Li, Y. Qin, et al., "Modulating the Stacking Model of Covalent Organic Framework Isomers with Different Generation Efficiencies of Reactive Oxygen Species," *ACS Applide Materials Interfaces* 13 (2021): 29471–29481.

33. U. A. Shah, S. Chen, G. M. G. Khalaf, Z. Jin, and H. Song, "Wide Bandgap Sb_2S_3 Solar Cells," *Advanced Functional Materials* 31 (2021): 2100265.

34. D. Liu, D. Zhang, Y. Wang, E. Liu, and H. Miao, "Fabricating S-Scheme Sb_2S_3@$CdSe_xS_{1-x}$ Quasi-One-Dimensional Heterojunction Photoanodes by In-Situ Growth Strategy Towards Photoelectrochemical Water Splitting," *Journal of Materials Science & Technology* 201 (2024): 250–260.

35. H. Deng, Y. Zeng, M. Ishaq, et al., "Quasiepitaxy Strategy for Efficient Full-Inorganic Sb_2S_3 Solar Cells," *Advanced Functional Materials* 29 (2019): 1901720.

36. D. Ma, M. Xu, L. Ding, et al., "Precise Regulation of Zn, S Dual Vacancies in $Zn_3In_2S_6$ Inducing Local Orientated Electrical Field for Photocatalytic H_2O_2 Generation," *Angewandte Chemie International Edition* 65 (2026): 21029.

37. C. Guo, F. Wang, A. Abdukayum, et al., "Axial and Asymmetric Coordination Coupling Adjust the Electronic Structure of Single-Atom Zinc Sites for Efficient Electroreduction of Carbon Dioxide," *Advanced Science* 12 (2025): 09698.

38. C. Feng, M. Hu, S. Zuo, et al., "Ru-O_V Site-Mediated Product Selectivity Switch for Overall Photocatalytic CO_2 Reduction," *Advanced Materials* 37 (2024): 2411813.

39. Q. Zhu, J. Su, G. Lin, et al., "Surface Indium Vacancies Promote Photocatalytic H_2O_2 Production over In_2S_3," *Nature Communications* 16 (2025): 10501.

40. K. Yang, L. Chen, K. Xiong, et al., "Bisite Sulfonate-Functionalized Covalent Organic Frameworks with Efficient and Dynamic Proton Transportation for Accelerating H_2O_2 Photosynthesis," *Advanced Functional Materials* 36 (2025): 20900.

41. S. Zhou, Q. Zhu, L. Kan, et al., "Achieving a Simultaneous Charge- and Energy-Involved Dual Channel Mechanism in Spirobifluorene-Based Conjugated Organic Polymers for Enhanced H_2O_2 Photosynthesis," *Journal of the American Chemical Society* 147 (2025): 44492–44506.

42. D. Chu, C. Xing, D. Sun, S. Li, and L. Ling, "Defective In_2S_3 with Proton-Enriched Interface Enable Sacrificial-Agent-Free Visible-Light Photocatalytic H_2O_2 Production," *Advanced Functional Materials* 36 (2025): 16500.

43. C. Zhao, A. Zhou, H. Li, et al., "Reversed Electron Transfer in Cu-TiO_2@$ZnIn_2S_4$ for Boosting Photocatalytic CO_2 Reduction," *Advanced Functional Materials* 36 (2025): 19072.

44. X. Wang, H. Zhang, Y. Huang, et al., "Nitrogen Defects and Interfacial Chemical Bonds in Fe Single-Site Mediated C_3N_4 with Rod-Like Fe_2O_3 Enhanced the S-Scheme Heterojunction for Efficient Energy Conversion," *Advanced Functional Materials* (2025): 2421847.

45. K. Li, W. You, Y. Zhu, et al., "Strong Electric Fields on Water Microdroplets Enable Near-Unity Selectivity in H_2O_2 Photosynthesis," *Journal of the American Chemical Society* 147 (2025): 36136–36145.

46. S. Zhou, X. Chen, L. Kan, et al., "Orthogonal Configurative Spirobifluorene-Based Conjugated Organic Polymers for Enhanced Water Oxidation Reaction to Boost H_2O_2 Photosynthesis," *Advanced Functional Materials* 36 (2025): 18050.

47. X. Sun, J. Yang, X. Zeng, et al., "Pairing Oxygen Reduction and Water Oxidation for Dual-Pathway H_2O_2 Production," *Angewandte Chemie International Edition* 63 (2024): 202414417.

48. H. Xu, Y. Wang, Y. Xu, et al., "Integrating Multipolar Structures and Carboxyl Groups in sp^2-Carbon Conjugated Covalent Organic Frameworks for Overall Photocatalytic Hydrogen Peroxide Production," *Angewandte Chemie International Edition* 63 (2024): 202408802.

49. Y. Tang, W. Wang, J. Ran, C. Peng, Z. Xu, and W. Chu, "The Evolution of Photocatalytic H_2O_2 Generation: From Pure Water to Natural Systems and Beyond," *Energy & Environmental Science* 17 (2024): 6482–6498.

50. Y. Huang, X. Wang, H. Zhang, et al., "Nb_2C MXene Quantum Dots Modulate Built-In Electric Field within Heterostructures for Efficient Solar-to-H_2O_2 Conversion from Seawater," *Applied Catalysis B: Environment and Energy* 371 (2025): 125262.

51. Q. L. Ma, J. Wei, Z. Lin, et al., "Enhanced Photocatalytic Performance of Ce^{3+}-Doped $ZnIn_2S_4$ Through Vacancy Engineering for Efficient Hydrogen Evolution and Pollutant Degradation," *Applied Catalysis B: Environment and Energy* 378 (2025): 125547.

52. X. L. Wu, S. Liu, Y. Li, et al., "Directional and Ultrafast Charge Transfer in Oxygen-Vacancy-Rich ZnO@Single-Atom Cobalt Core-Shell Junction for Photo-Fenton Like Reaction," *Angewandte Chemie International Edition* 62 (2023): 202305639.

53. Y. Liu, J. Shi, C. Li, et al., "Rational Regulation of Vacancy Species to Manage Migration Paths of Carriers in MoS_2/TiO_2 Heterojunctions for Efficient Photocatalytic H_2 Generation," *International Journal of Hydrogen Energy* 47 (2022): 28845–28858.

54. W. Chi, B. Liu, C. Pan, J. Zhang, Y. Dong, and Y. Zhu, "Customizing Oxygen Reduction Reaction Pathways for High-Efficiency H_2O_2 Photosynthesis by Anionic Intermediate-Generating Polymer Photocatalysts," *Advanced Functional Materials* 35 (2025): 13175.

55. X. Zheng, Z. Pan, J. J. M. Vequizo, et al., "Nanoscale Reduction-Site-Selective Oxygen Regulation for Promoting Hydrogen Peroxide Production," *Nature Communications* 17 (2025): 269.

56. J. Tang, J. Li, L. Li, et al., "A Low-Temperature Solar Salt Approach to Fabricate Crystalline Polymeric Carbon Nitride for H_2O_2 Efficient Photosynthesis," *Advanced Science* 13 (2026): 12549.

57. C. Yang, S. Wan, B. Zhu, J. Yu, and S. Cao, "Calcination-Regulated Microstructures of Donor-Acceptor Polymers towards Enhanced and Stable Photocatalytic H_2O_2 Production in Pure Water," *Angewandte Chemie International Edition* 61 (2022): 202208438.

58. Y. Y. Tang, X. Luo, R. Q. Xia, et al., "Molecular Engineering of Metal-Organic Frameworks for Boosting Photocatalytic Hydrogen Peroxide Production," *Angewandte Chemie International Edition* 63 (2024): 202408186.

59. Y. Luo, B. Zhang, C. Liu, et al., "Sulfone-Modified Covalent Organic Frameworks Enabling Efficient Photocatalytic Hydrogen Peroxide Generation via One-Step Two Electron O_2 Reduction," *Angewandte Chemie International Edition* 62 (2023): 202305355.

60. H. Li, J. Zhang, B. Zhu, et al., "Orchestrating Ti-S and Ni-S Bonding Interfaces for Accelerated Charge Transfer in a S-Scheme Photocatalyst," *Advanced Functional Materials* 36 (2025): 21318.

61. W. Wang, Z. Chen, C. Li, et al., "Graphene Quantum Dot-Modified $Mn_{0.2}Cd_{0.8}S$ for Efficient Overall Photosynthesis of H_2O_2," *Advanced Functional Materials* 35 (2025): 2422307.

62. Y. Xi, C. Zhang, W. Tu, et al., "Modulating Active Hydrogen Supply and O_2 Adsorption: Sulfur Vacancy Matters for Boosting H_2O_2 Photosynthesis Performance," *Angewandte Chemie International Edition* 64 (2025): 202505046.

63. L. Fang, S. Qiu, H. Xu, T. Ye, and L. Li, "Encapsulation of Single-Atoms into Covalent Organic Frameworks for Highly Efficient and Persistent H_2O_2 Photosynthesis via Biphasic Flow Chemistry," *Advanced Functional Materials* 35 (2025): 2504676.

64. J. L. Zhou, Y. F. Mu, M. Qiao, et al., "Unlocking One-Step Two-Electron Oxygen Reduction via Metalloid Boron-Modified $Zn_3In_2S_6$ for Efficient H_2O_2 Photosynthesis," *Angewandte Chemie International Edition* 64 (2025): 202506963.

65. D. Wang, F. Tan, W. Zhao, et al., "Develop Complex Photocatalytic System of D-π-A-type Conjugated Porous Polymers and Benzyl Alcohol Mediated Autocatalysis for Practical Artificial Photosynthesis of H_2O_2," *Angewandte Chemie International Edition* 64 (2025): 202425017.

66. X. Fang, B. Li, J. Huang, et al., "Sodium/Potassium Poly(heptazine imide) with an Electron Sink Effect for Hydrogen Peroxide Photosynthesis," *Energy & Environmental Science* 18 (2025): 6202–6213.

Supporting Information

Additional supporting information can be found online in the Supporting Information section.

Supporting File: adfm77350-sup-0001-SuppMat.docx.